Available online at www.sciencedirect.com
ScienceDirect
Electrochimica Acta 53 (2008) 3279–3295
ELECTROCHIMICA Acta
www.elsevier.com/locate/electacta

Degradation mechanism study of perfluorinated proton exchange membrane under fuel cell operating conditions

Nagappan Ramaswamy, Nazih Hakim, Sanjeev Mukerjee *

Department of Chemistry and Chemical Biology, Northeastern University, Boston, MA 02115, USA

Received 3 August 2007; received in revised form 5 November 2007; accepted 7 November 2007
Available online 13 November 2007

Abstract

Perfluorinated sulfonic acid proton exchange membranes are in the forefront as solid electrolytes for fuel cell applications. Although expensive, its potential utilization in commercial fuel cells can be validated provided it can be established that it is highly durable. In this context, peroxide radical-initiated attack of the membrane electrode interface is one of the key issues requiring further systematic investigation under fuel cell operating conditions, to better determine the fundamental degradation mechanism. In this study, we attempt to analyze the durability of the membrane electrode assembly (MEA) made with different commercial electrodes from the perspective of peroxide radical-initiated chemical attack on the electrode/electrolyte interface and find the pathway of membrane degradation as well. A novel segmented fuel cell is employed for durability characterization, and use of this cell and pre and post analysis of the membrane are presented. Correlation of membrane degradation data with the peroxide yield determined by RRDE experiments is obtained. This method is able to separate the membrane evaluation process into cathode and anode aspects. Fenton type mechanism of peroxide radical generation from H_2O_2 formed due to two-electron pathway of ORR is found to be the dominant membrane degrading factor.

Keywords: PEMFC durability; Nafion membrane degradation; ORR and peroxide yield; FTIR of Nafion; Array electrode assembly fuel cell

1. Introduction

Widespread commercialization of PEMFC's is strongly predicated on component costs and striking an optimum balance between its performance and durability. Although extensive research seeking enhancement in performance of PEMFC's is available (decreasing noble metal catalyst loading, improving reactant and catalyst utilization, developing new polymer electrolytes, non-noble metal catalysts, improving stack and flow field designs) extensive investigations of durability issues has been relatively recent mainly because of the test duration requirements and complexity of analysis brought on by existence of parallel processes and inability to perform in-situ, nondestructive analysis of the key components[1]. Since the MEA being the heart of an operating PEMFC where electrochemical energy conversion takes place, it is more prone to chemical and electrochemical degradation and remains as the biggest determinant in the extent of losses in fuel cell performance. Degradation of MEA components are broadly understood to be due to (i) electrocatalyst sintering via (a) thermal induced coalescence and growth following surface migration over the carbon support material, and (b) 'Ostwald Ripening' which follows a dissolution redeposition mechanism; (ii) platinum particle agglomeration triggered by corrosion of carbon support; (iii) electrocatalyst poisoning, surface segregation and morphology changes due to presence of strong surface chemisorption by species such as CO, sulfur compounds, products of methanol oxidation, etc.; (iv) self segregation of elements in mixed metal oxides or alloys brought on by potential excursions, etc.; and (v) degradation of ion conducting component including membrane and smaller aggregates present along side the electrocatalyst in the reaction layer due to free radical species generated at the interface. All these degradation processes are a strong function of operating conditions such as temperature, partial pressures, relative humidity, overpotentials, etc.

Perfluorosulfonated Nafion membranes (Fig. 1) have received priority in durability studies [2,3] although sulfonated nonfluorinated aromatic membranes [4] and composite

* Corresponding author. Tel.: +1 617 373 2382; fax: +1 617 373 8949.
E-mail address: s.mukerjee@neu.edu (S. Mukerjee).

0013-4686/$ – see front matter © 2007 Elsevier Ltd. All rights reserved.
doi:10.1016/j.electacta.2007.11.010

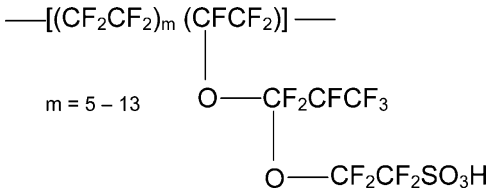

Fig. 1. Chemical structure of Nafion® 112.

membranes [5] represent one large group of promising candidates. Apart from physical, mechanical degradations such as membrane thinning and pinhole formations as a result of hydrolytic decomposition at elevated temperature and induced stresses, peroxide lead free radical attack and subsequent degradations are of more immediate importance due to potential of rapid irreversible damage. Oxygen reduction reaction (ORR) is a multi electron transfer process which involves several elementary steps with corresponding generation of intermediate species. A more typical scheme representing the overall oxygen reduction reaction in acid medium is shown below [6,7].

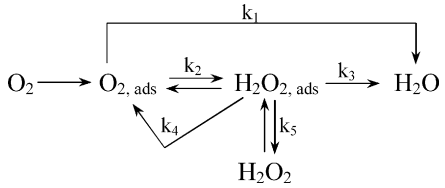

Noteworthy feature in the above scheme is that the overall mechanism of direct electrochemical reduction of O_2 to water ('direct' $4e^-$ pathway) is a parallel process part of which proceeds via the formation of H_2O_2 intermediate ($2e^-$ reduction pathway). Formation of H_2O_2 has been confirmed using a microelectrode in an operating fuel cell [8] and Scherer [9] detected the presence of H_2O_2 in outlet stream of operating PEM fuel cells with Nafion membrane. Besides the formation of peroxide radical due to the incomplete reduction of oxygen [10–12] (i.e., two-electron reduction occurring in a parallel pathway to the four-electron reduction) at a fuel cell cathode it can also be generated at open-circuit conditions with interaction of hydrogen and crossover oxygen at the anode catalyst–membrane interface [9,13–15]. It is noted that, membrane degradation is initiated by the free radicals generated by Fenton type metal cation catalyzed decomposition of hydrogen peroxide [16–19] as shown below:

$$M^{2+} + H_2O_2 \rightarrow M^{3+} + {}^{\bullet}OH + OH^-$$

$$M^{3+} + H_2O_2 \rightarrow M^{2+} + {}^{\bullet}OOH + OH^+$$

PEM easily absorbs ionic contaminants due to the stronger affinity of foreign cations with the sulfonic acid group than that of H^+ [19]. Possible sources of ionic contaminants are the carbon support, gas diffusion electrodes, humidifying bottles, corrosion of tubing or stack materials, and other fuel cell hardware. Especially, the iron contamination from fuel cell end plate has been found to be the key supplier of foreign ion contamination [16].

From the perspective of peroxide radical attack of the membrane, hydroxy ($^{\bullet}OH$) and hydroperoxy ($^{\bullet}OOH$) radicals are the most likely initiators of membrane chemical decomposition [13] as they are some of the most reactive chemical species known [20–22]. Radical-initiated attack leads to the breakage of perfluorocarbon backbone in Nafion membranes and sulphonate groups which directly affect mechanical strength and proton conductivity of the membranes [23], leading to increase in total cell resistance and a loss in net power output. Also the degradation of polymer membrane is very much dependent on the operating conditions such as temperature [24], and humidity [1,25], freeze–thaw cycling, transient operation, fuel or oxidant starvation, start-up and shutdown. Earlier Fenton's test or similar other tests have been used to study membrane degradation, in which the membrane is directly exposed to hydrogen peroxide and ppm quantities of cationic contaminants. Although Fenton's test is straightforward and has been considered as benchmark for PEM durability evaluation, it has inherent limitations. Deterioration of membrane in such a test involves no electrode process and incomparable with variations in fuel cell working conditions such as operating potential, relative humidity, fuel and oxidant starvation, etc. Such tests are controversial as they do not simulate accurate fuel cell operating environments. An alternative approach that has more practical relevance is to run a long-term fuel cell test and conduct post-mortem analysis to study the changes in membrane properties. However, in a conventional sense, this method requires a minimum of hundreds of hours in order to obtain detectable degradation. Testing fuel cells for such lengthy periods of times is expensive and generally impractical; further, the stability of other fuel cell components could become the dominating source of performance degradation during such tests.

A systematic investigation of degradation of polymer membrane at fuel cell operating conditions is highly warranted in order to further the fundamental understanding and substantiate PEMFC technology as an alternative renewable energy source. So, in this work, we attempt to analyze the durability of MEA from the perspective of radical-initiated chemical attack of the membrane. From an overall perspective the objectives of this investigation were to understand the following: (i) extent of membrane degradation as a function of cathode and anode electrode polarization conditions, effect of (ii) temperature; (iii) catalysts loading; and (iv) comparison of Pt versus Pt-alloys, in the case of the latter distinction between catalysts containing alloying element on the surface versus alloys possessing a Pt rich outer layer have been investigated. These were studied using our novel segmented cell design [4] for durability characterization. The unique segmented fuel cell design and experimental protocol as described in detail earlier [4] enables multiple working electrodes to be analyzed on the same membrane, such that specific half-cell (anode and cathode) conditions and choice of electrocatalysts as well as overpotentials can be invoked under actual fuel cell operating environments. This segmented cell experimental protocol therefore allows for measurement of membrane degradation in terms of losses in its ionic conduction as well as within the bulk of its structure from identification of point of chain scission. These are achieved by comparison of pre- and post-mortem data from four point proton conductivity measurements (in-plane and through plane), ion exchange capacity and infrared data, respectively. Membrane degradation is then correlated with directly measured peroxide

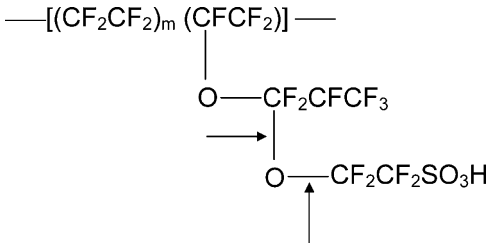

Fig. 2. Sensitive sites for radical attack in Nafion® 112 [Arrows indicate ether bond A as the vulnerable site as labeled in Fig. 11].

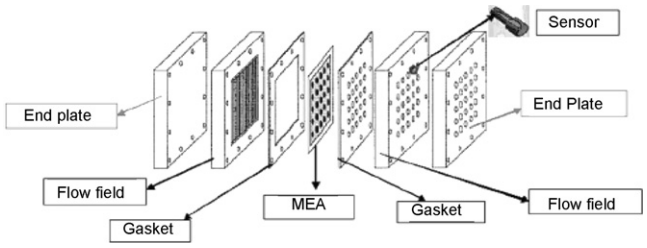

Fig. 3. Segmented array fuel cell assembly designed for testing multiple working electrodes, each with individual reference electrodes and a common counter.

yield values for various electrocatalysts during oxygen reduction using rotating ring-disk electrode technique. The objective is to therefore correlate peroxide yields with membrane degradation and understand membrane durability as a function of temperature, catalyst loading, electrode overpotentials, pure Pt versus Pt-alloy electrocatalyst, nature of polymer chain scission (point of radical-initiated attack) and overall polymer breakdown.

2. Experimental

2.1. Physicochemical characterization

X-ray diffraction (XRD, model D/MAX-2200T) was used to characterize the crystal structure, phase purity, and particle size of the catalysts. The measurements were made with a Rigaku diffractometer, at 46 kV and 40 mA, fitted with Cu K_α radiation source, $\lambda_{Cu\,K_\alpha} = 1.5406$ Å. The diffraction patterns were recorded with a scan rate of 0.400°/min between 10° and 100°. The analysis of the XRD data was carried out using the "Cell Refinement" package. The average crystal size of the catalyst was determined using a Scherrer crystallite size broadening model. Micro-structural characterizations were carried out with cold field emission high resolution scanning electron microscope (HRSEM), Hitachi (model S-4800), to take high resolution topographical micrographs of the catalyst samples. HRSEM micrographs are very useful in analyzing the morphology of the carbon support, the crystallite size distribution of the catalysts, and the coverage of the catalyst nano-particles over the support. Attached to the SEM unit is an energy dispersion X-ray spectrometer (EDS, EDS-GENESIS HITACHI S-4800), equipped with a Cu filter and a liquid nitrogen-cooled Si(Li) detector, and it was used to measure the composition of the alloyed catalysts at an acceleration voltage of 25 kV.

2.2. Electrochemical characterization

All electrochemical measurements were made at room temperature using a rotating ring-disk electrode setup from Pine Instruments connected to an Autolab (Ecochemie Inc., model—PGSTAT 30) potentiostat equipped with a bipotentiostat interface. All potentials in acidic and alkaline solutions were measured with respect to sealed hydrogen electrode (RHE) and Hg/HgO reference electrode, respectively. Detailed methodologies are given elsewhere [26]. Briefly, ink formulation consisted of sonicating the electrocatalyst powder with an appropriate quantity of water, isopropanol and small quantity of 5 wt% Nafion® solution as a binder. Four-microlitre aliquot of catalysts ink with a target Pt metal loading of 14 μg/cm^2 was dropped on glassy carbon (GC) disk (0.196 cm^2) substrate. 1M $HClO_4$ and 1M KOH were used as the electrolytes. In a separate experiment, a study for determining optimal electrocatalyst loading on GC disk was performed. Ideal loading of 14 μg/cm^2 (Pt) was determined from the point of inflection of a plot of mass transport normalized current (at 900 rpm) for ORR versus loading (Pt metal).

2.3. Segmented cell design

Durability experiments were performed using a modified fuel cell hardware based on a "high throughput screening fuel cell assembly" (NuVant System, Inc., IL, USA) [27]. Fig. 3 shows the original schematic of the fuel cell assembly. Its key components include an electronically conducting flow field block and

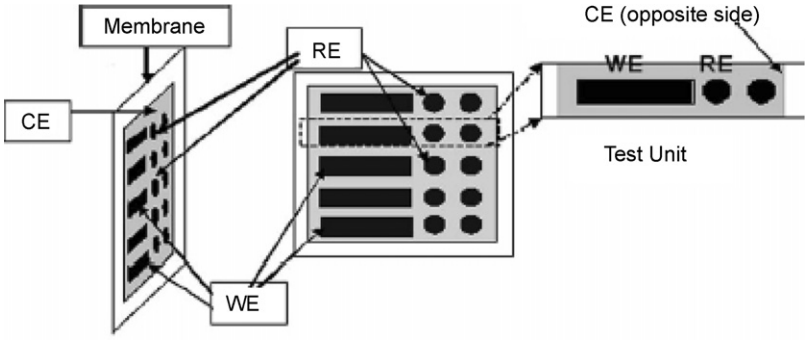

Fig. 4. Design of MEA for durability test showing the five individual working electrodes (WEs) each with their reference electrode (RE) arrangement and common counter electrode (CE).

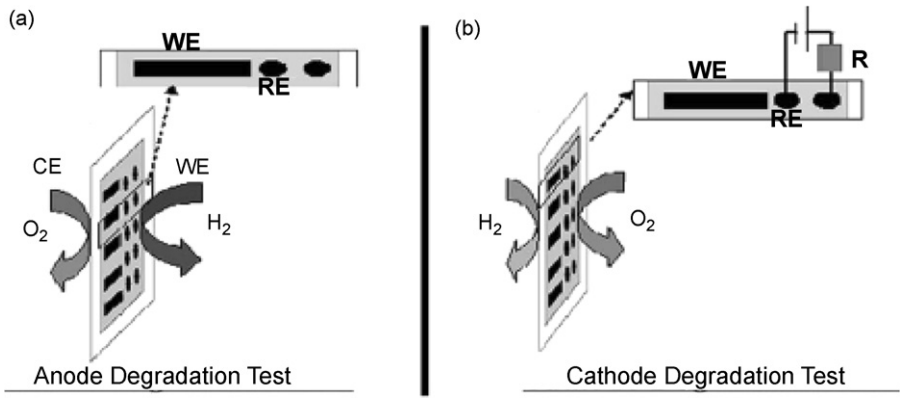

Fig. 5. Half-cell configuration of anode and cathode-side degradation tests.

an electronically insulating array block on the opposite side of the MEA. The array block has 25 sensors glued into the block on the opposite side facing one of the testing spots on the array MEA and a pin jack on the other side used for electrical connection. The heating control and gas supplies to this fuel cell were built in-house to enable the cell to run at ambient pressure and constant temperature up to 80 °C [28]. Gases were passed through humidification bottles, which were kept at a temperature 10 °C higher than that of the cell in order to ensure the 100% humidification of the MEA.

The MEAs in this work were customized for the purpose of the durability tests. As shown in Fig. 4, the MEA consists of the membrane of interest with a size of 11 cm × 11 cm. Attached to one side of the membrane is a titanium mesh common counter electrode (CE). On the other side, the testing area of the MEA is divided into five testing units. Each unit has a strip of electrode as the working electrode (WE), and two disk electrodes for building the reference electrode (RE) of this unit. This design enables a simultaneous evaluation of five catalyst samples of geometric area 5 cm^2 (5 cm × 1 cm) at each run under same operating conditions. A multi-channel Arbin (BT2000) Testing System (Arbin Instruments, TX) was used for polarization of the individual working electrodes.

2.4. Durability test design criteria

In prior publications concerning the susceptibility of PEM's to radical-initiated chemical attack, fuel cell experiments performed with either single cell or multi-cell stack played an important role. These extended life testing reflected indeed the combined impact from various sources (fuel cell component configuration, MEA fabrication, operating conditions, thermal and load cycles, impurities, and uniformity, etc.) on the lifetime of the membrane. However, the interplay of these factors leads to inevitable difficulties in interpreting and reproducing the data and inability to assign the observed membrane failure to one particular factor without taking other possible triggers and/or enhancers into account. From this point of view, a unique membrane durability test was designed so as to enable data interpretation. To understand the radical-induced membrane degradation during fuel cell operation, two types of durability test were tailored for examining the proposed mechanisms: (a) cathode-side durability test; and (b) anode-side durability test.

2.4.1. Anode-side durability test

The 'anode (hydrogen) side degradation mechanism' as proposed earlier [13] is based on the premise that during fuel cell operation, unreacted molecular O_2 from the cathode feed permeates through the membrane and reacts with atomic hydrogen chemisorbed on the surface of the anode platinum catalyst, thus producing hydrogen peroxide or free radicals. Any peroxides formed at this interface in conjunction with traces of transition metal ions [Fe^{2+}, Cu^{2+}, . . .found in MEA and/or catalyst support (carbon black)] results in formation of free radicals. The possible reactions involved in this mechanism are [13]:

$$H_2 \rightarrow 2H_{ads}(\text{onPtorPt/Mcatalyst})$$

$$H_{ads} + O_2(\text{diffusedfromcathodeside}) \rightarrow HOO^{\bullet}$$

$$HOO^{\bullet} + H^{+} \rightarrow H_2O_2$$

$$M^{2+} + H_2O_2 \rightarrow M^{3+} + {}^{\bullet}OH + OH^{-}$$

$$M^{3+} + H_2O_2 \rightarrow M^{2+} + {}^{\bullet}OOH + OH^{-}$$

This proposed mechanism has been suggested on the basis of tests in regular fuel cell setups under open-circuit potential (OCP) conditions in prior publications [14,25]. However, the parallel process involving interaction of adsorbed oxygen at the cathode (at or near OCP conditions) and cross over hydrogen resulting in free radical formation cannot be ruled out. This has been pointed out in an earlier publication [25]. Therefore, it is imperative for appropriate experimental design for proper data interpretation. An earlier attempt to understand the extent of this mechanism involved providing the electrolyte/catalyst interface a predominantly H_2 environment consisting of a small amount of O_2. For example, to induce degradation of water soluble polystyrene sulfonic acid [used as a model compound for hydrated polystyrenesulfonic acid (PSSA) membrane], Hodgen et al. [29] purged hydrogen gas containing 5% oxygen through a PSSA polymer solution at the rate of 1.5 cm^3/s in the presence of platinized platinum. Clearly this method deviated from fuel cell

Table 1
Basic membrane properties of Nafion® 112 showing ion exchange capacity (η), membrane thickness, glass transition temperature (T_g), proton conductivity (σ)

Membrane	Ion exchange capacity (η) (mEq/g)	Proton conductivity (σ) (S/cm at 22 °C, 100% RH)	Thickness (mm)	T_g (C)
Nafion® 112	0.91	0.097	0.0508	140

configuration; also it failed to mirror the O_2 crossover behavior, because O_2 permeability through the membrane changes dramatically with the chemistry of polymer as well as temperature and hydration [30].

In order to investigate this mechanism under fuel cell-like conditions in the absence of interference from reactions of O_2 with crossover hydrogen, our approach involved conducting tests in the aforementioned fuel cell device running with pure hydrogen and pure oxygen (in a normal fuel cell mode) at ambient pressure. As shown in Fig. 5a, humidified hydrogen was passed through the catalyzed working electrode which also provided reference electrode for the MEA, and humidified oxygen was passed through the non-catalyzed counter electrode side in order to enable oxygen diffusion through the membrane to the working electrode side depending on its permeability at the operating condition of the fuel cell. After full humidification of the MEA (on reaching equilibrium conditions), the working electrodes were either held at the typical anode potential of the PEMFC [0.1–0.2 V, versus a reference hydrogen electrode (RHE)] or left in OCP condition for a fixed period of time. After the test, membranes in contact with the working electrodes were detached for postmortem analysis. The results were then compared with the corresponding properties of the non-degraded membrane before the test (Table 1). Further, it is also noted that, the possibility of H_2 cross over to the cathode side to cause analogous degradation did not find favor in the literature because of the fact that H_2 utilization efficiency on the anode side is sufficiently high enough evidenced by low magnitude of H_2 crossover current density ($\sim$1–3 mA/cm^2) reported widely in the literature [31–34] and measured in our lab as well. Furthermore, the counter electrode side with O_2 flow was a non-catalyzed carbon electrode and hence lacked the reaction centers afforded conventionally by Pt.

2.4.2. Cathode-side durability test

Recent publication [12,13,16,23,35,36] suggested that the vulnerable location for radical attack in a MEA is at the cathode (oxygen) side. This mechanism is based on the proposition of oxygen reduction reaction (ORR) at the cathode of PEMFC proceeding via a parallel pathway where a two-electron reduction of oxygen occurs simultaneously with the formation of H_2O_2 intermediates [37] along with the predominant four-electron reduction to H_2O; the peroxides then react with trace transition metals ions (Fe^{2+}, $Cu^{2+}\cdots$ found in membrane and/or carbon black catalysts support) to form radicals:

$$O_2 + 2H^+ + 2e^- \rightarrow H_2O_2 \quad (1)$$

$$M^{2+} + H_2O_2 \rightarrow M^{3+} + {}^{\bullet}OH + OH^- \quad (2)$$

$$M^{3+} + H_2O_2 \rightarrow M^{2+} + {}^{\bullet}OOH + H^+ \quad (3)$$

It has been pointed out that the metal ion and H_2O_2 concentrations necessary for the occurrence of hydroxyl radical can be very low (<10–25 mg/L H_2O_2 and 1 part Fe per 5–25 parts of H_2O_2 (wt/wt) [38])

Fig. 5b shows our cathode durability test arrangement. The cell is operated on pure oxygen and pure nitrogen at ambient pressure. Humidified oxygen is passed through the working electrode side of the cell; humidified nitrogen, which is inert therefore only functions to hydrate the MEA, is passed through the counter electrode side so that water molecules carried by nitrogen undergo oxidation at the counter electrode and provide protons that pass through the membrane to the working electrode side purged with humidified oxygen. This design emulates an operating fuel cell except for suppressing the passage of hydrogen on the anode side. The reference electrode is a solid-state dynamic hydrogen electrode (DHE) [39], which is constructed by connecting two disk electrodes (E-TEK 30% Pt/C electrode) to power supply of 1.7 V. After full hydration of the MEA, the potential of the working electrode could be set (versus DHE) for 24–48 h time period at different potentials. Cathode-side membrane degradation was studied both at normal fuel cell cathode operating potentials of 0.6 V and 0.7 V versus DHE and also accelerated conditions of membrane degradation was achieved at a cathode potential of 0.4 V versus DHE in this present study. Pre- and post-test analysis of the membrane in contact with the working electrode is conducted. The results were then compared with the corresponding properties of the membrane before the test (Table 1).

2.5. MEA fabrication

Working electrodes were selected from commercial ETEK-BASF 30% Pt/C, 60% Pt/C, 30% Pt_2Co/C and 30% Pt_3Co/C. Material for the reference electrode was 30% Pt/C electrode (E-TEK-BASF). The counter electrode for the anode-side durability test was non-catalyzed carbon gas diffusion electrode (E-TEK-BASF). For the cathode degradation test 0.6 mg_{Pt}/cm^2 of 80% Pt/C (ETEK-BASF) was used as the catalyst and titanium mesh for current collection.

Working electrodes were prepared by sonicating for 20 min an appropriate amount of water-wetted catalyst with 5 wt% Nafion® 1100EW (Ion-Power, Inc. – New Castle, DE) and isopropanol. All working electrode catalyst loading was 0.4 mg_{Pt}/cm^2. The resulting catalyst ink was then sprayed on the commercial carbon gas diffusion electrode (single sided ELAT, E-TEK) and then dried in oven at 60 °C for 60 min. For electrodes obtained from commercial vendors, a thin layer of Nafion® ionomer solution was brushed on the electrode surface and then dried in oven. Typical loading of ionomer layer was in the range of 0.8–1.0 mg/cm^2. MEAs

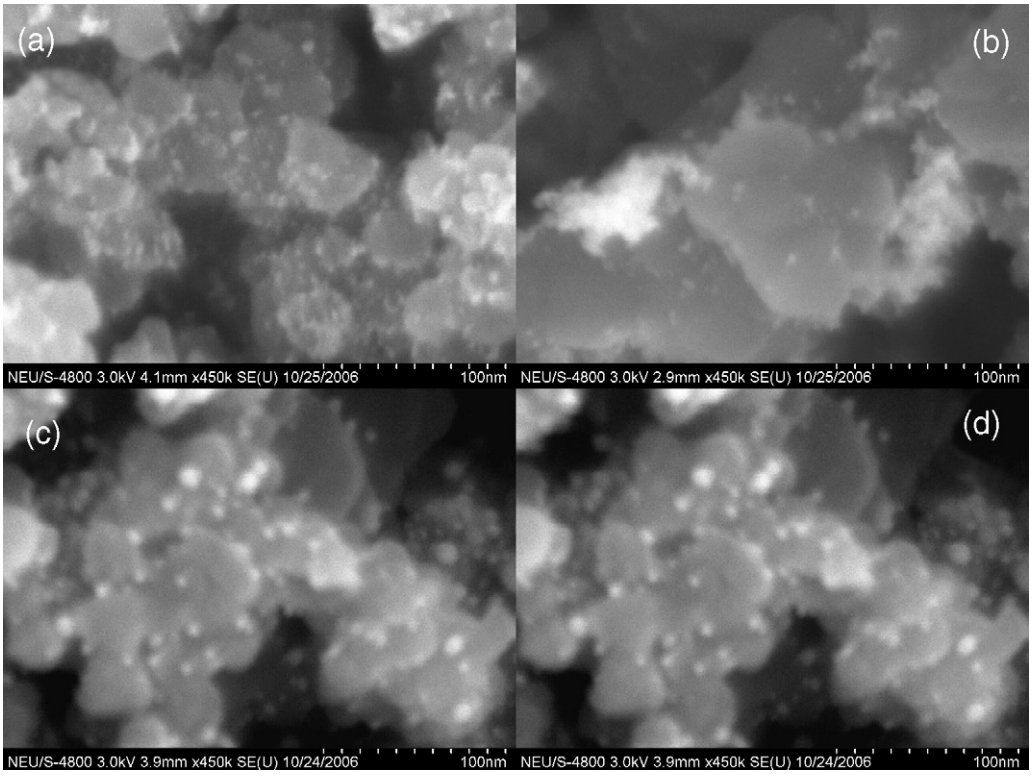

Fig. 6. SEM images of PEMEAS Pt and Pt-alloy catalysts employed in this study: (a) 30 wt% Pt/C; (b) 60 wt% Pt/C; (c) 30 wt% Pt_2Co/C; and (d) 30 wt% Pt_3Co/C.

were prepared by hot-pressing the electrodes to the polymer membrane according to procedures described in detail earlier [28].

2.6. Characterization techniques

After the durability experiment, the MEA was uninstalled from the cell, and the working electrode portions were carefully cut off from the MEA with the appropriate working electrode side carefully labeled. The samples were then dipped in anhydrous methanol for a short fraction of a second to enable peeling of the electrodes from the membrane. The membrane samples so obtained, typically 1 cm × 5 cm, were then washed thoroughly with deionized water before performing the following analysis.

2.6.1. Fourier-transform infrared spectroscopy

Fourier transform infrared spectroscopy (FTIR) is a handy, nondestructive technique to probe changes in membrane chemistry due to degradation, used in numerous studies [40,41] and to determine the microstructure of Nafion® in prior PEM stability studies [14,15]. In this work, infrared spectra, plays an important role in revealing the chemical processes underlying degradation. Due to the thickness of the sample, attenuated total reflection (ATR) mode was employed instead of transmission mode. IR spectra were recorded with either Mattson RS-2 FTIR instrument equipped with a pike MIRacle ATR unit with 45° ZnSe ATR Crystal or Bio-Rad FTS6000 FTIR instrument with 45° Ge ATR crystal. The reason for using two different crystals is to exploit the difference in IR penetration depth that they provide due to difference in refractive index of ZnSe and Ge. ZnSe provides a penetration depth of 1.7–2 μm from the membrane surface whereas Ge has only 0.65–0.7 μm from the membrane surface in the IR wavenumber region of ∼400–4000 cm^{-1} [42]. For measurement, the dried sample (24 h in vacuum at 60 °C) was pressed against the ATR crystal with the help of a force-sensing pressure applicator. All spectra were collected from 400 scans at 4-cm^{-1} resolution. Dry nitrogen gas was purged around the sample during the measurement to eliminate moisture in the air. Linear background correction in the spectra was attained manually.

Table 2
Physicochemical characterization of Pt and Pt-alloy catalysts using SEM/EDS

Catalyst[a]	EDS elemental composition	Average size (Å) (XRD)	Lattice parameter (Å)
30 wt% Pt/C	–	27	3.934 (Fm3m)
60 wt% Pt/C	–	36	3.934 (Fm3m)
30 wt% Pt_3Co/C	Co = %24 ± 1, Pt = %76 ± 1	55	3.855 (Fm3m)
30 wt% Pt_2Co/C	Co = %32 ± 1, Pt = %68 ± 1	70	3.81 (Fm3m)

[a] All are commercial PEMEAS catalysts supported on Vulcan XC-72 Carbon.

2.6.2. Conductivity measurement

Proton conductivity was determined from a fully humidified membrane at room temperature using four-probe conductivity cell setup described in our prior publication [43]. Measurements were carried out with a digital potentiostat/galvanostat (AUTOLAB model PGSTAT30 equipped with FRA model, Ecochemie B.V.).

2.6.3. Ion exchange capacity (IEC)

Ion exchange capacity (IEC) defined as the ratio of moles of sulfonate ion exchange sites to the dry of Nafion® is expressed in mEq/g and were measured using standard methods, which involved equilibrating known amount of H^+ form of the membrane in measured volume of a standard solution of 3 M NaCl at 100 °C for 10 h to allow for the exchange with H^+ ions. This solution was then titrated to a phenolphthalein end-point with a standard NaOH solution.

3. Results and discussion

3.1. Physicochemical characterization (SEM and XRD)

HRSEM micrographs for the electrocatalysts of Pt, and Pt–Co are shown in Fig. 6. These images show that statistically overwhelming number of observable particles have sizes in the range <3 nm for 30%Pt/C and in the range of 2–5 nm for 60%Pt/C. Particle size distribution for Pt–Co alloys exhibited a wider range, and particle size variation from 2 nm to 10 nm was observed as compared with the pure Pt catalyst. Except for the 60%Pt/C, where the nano-particles of this catalyst aggregate, the catalyst particles for the rest of the samples are well dispersed and distributed on the carbon support. Along with the SEM patterns the fluorescence signal was analyzed using EDAX analyzer and software (EDS-GENESIS, HITACHI S-4800). As shown in Table 2, the atomic composition of the two supported Pt–Co alloys show that in comparison to Pt_3Co whose elemental composition is 75:25, the Pt_2Co sample exhibits ~70:30 ratio,

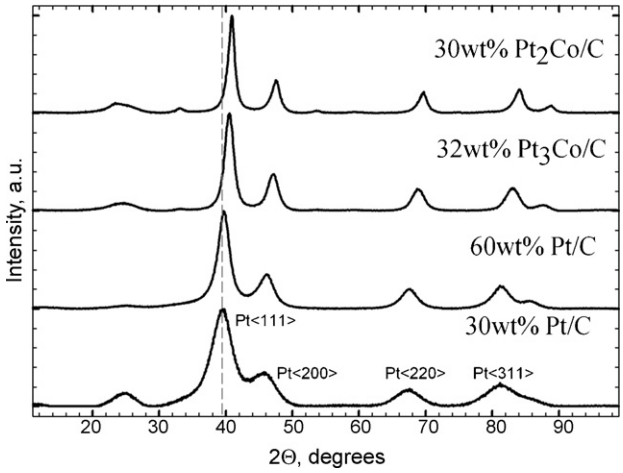

Fig. 7. X-ray diffractograms of the Pt and Pt-alloy catalysts used in this study.

thereby showing very good correspondence with the nominal composition. X-ray diffraction patterns of the supported electrocatalysts, Pt, Pt–Co mixtures scanned at 2θ angles over a range of 10–100° are shown in Fig. 7. The broad-based diffraction peak at $\sim 2\theta = 24.6°$ for all types of catalysts arises from that of the carbon support. In Fig. 7, the two Pt catalysts show the typical platinum peaks at 2θ position of ⟨1 1 1⟩, ⟨2 0 0⟩, ⟨2 2 0⟩, ⟨3 1 1⟩, and ⟨2 2 2⟩; whereas the Pt–Co peaks position are shifted slightly higher in 2θ values showing an appropriate reduction in lattice parameters as a result of addition of Co in the unit cell structure showing a clear indication of Pt–Co alloy formation. The approximate average particle sizes of the carbon-supported catalysts were determined by using the Scherrer equation [44], which relates crystallite size to the line broadening of the peaks. Although not accurate for particles either (<5 nm) or above (>50 nm), XRD still constitutes one effective tool for estimating catalyst particle sizes usually in the range of 5–50 nm. However, these particle sizes reflect exclusively the diffracting domains and so all amorphous components are excluded. The average particle sizes, based on the peak width of the ⟨1 1 1⟩, ⟨2 0 0⟩,

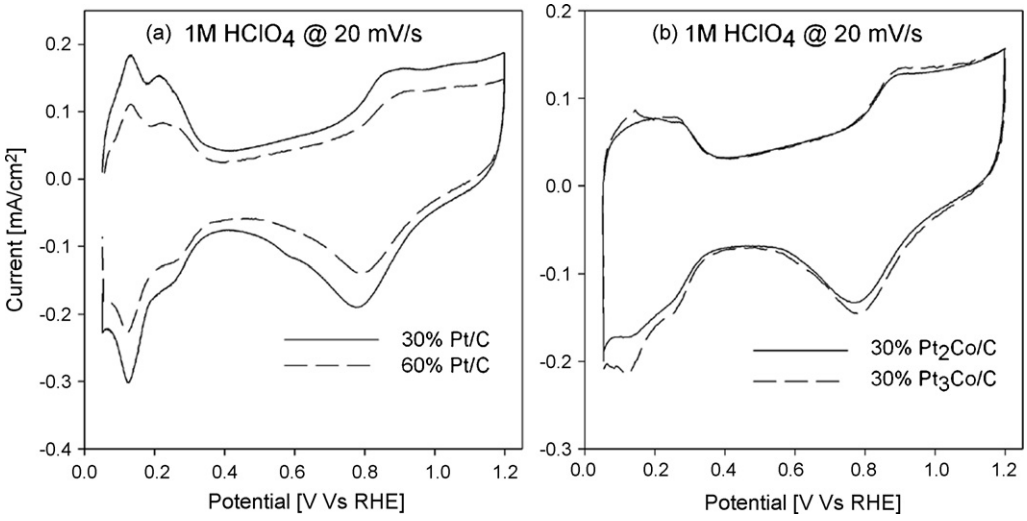

Fig. 8. Cyclic voltammograms in oxygen-free 1 M $HClO_4$ at room temperature for (a) Pt and (b) Pt-alloy catalysts used in this study on a glassy carbon disk at 20 mV/s. Current densities based on geometric electrode area.

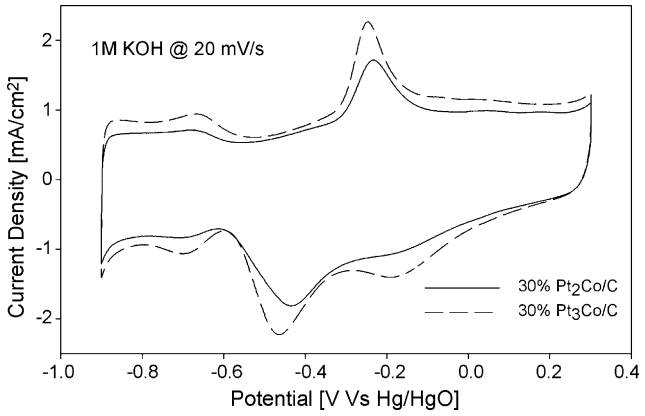

Fig. 9. Cyclic voltammograms in oxygen-free 1 M KOH at room temperature for 30% Pt_2Co/C and 30% Pt_3Co/C catalysts at 20 mV/s; current densities are based on geometric electrode surface area of the glassy carbon disk.

and ⟨2 2 0⟩ diffraction lines and lattice parameters are presented in Table 2. There is a broad agreement between the particle sizes obtained from SEM and XRD analysis, thereby indicating a high degree of crystalline character to the supported Pt and Pt-alloy naonoparticles. The lattice parameter obtained from the XRD patterns indexed to a face-center cubic (fcc) structure was 3.9238 Å which is in good agreement with the literature value of 3.9239 Å. The Pt–Co binary mixtures have lower lattice parameter values than the corresponding pure platinum, and increasing the atomic content of cobalt in the mixture decreases the lattice parameter values, since the atomic radius of cobalt is smaller than platinum and the decrease in lattice parameter indicates alloying of the metals where cobalt enters the platinum lattice by substitution in to octahedral sites [45].

3.2. Electrochemical measurements—cyclic voltammetry

Cyclic voltammetry (CV) was used to characterize the catalysts in argon purged 1M $HClO_4$ at room temperature by cycling between 0.05 V and 1.2 V versus RHE. Also CVs were recorded in 1 M KOH electrolyte to investigate the electrochemical behavior of cobalt in Pt–Co alloys used in this study. This was especially useful in determining presence of surface Co as characterized by typical redox peaks in alkaline electrolytes. The resulting voltammograms in oxygen-free acidic and alkaline electrolytes taken at 20 mV/s with a loading of 14 $\mu g_{Pt}/cm^2$ are shown in Figs. 8 and 9. The electrochemically active surface area of the catalysts was also estimated from the integrated charge in the H adsorption/desorption region of the CVs and are shown in Table 3. Cyclic voltammograms show that the carbon-supported Pt particles possess some degree of low coordinated crystal planes, and hence the hydrogen adsorption/desorption features between 0.4 V and 0.0 V versus RHE are different from the CV expected of a bulk pc-Pt electrode. The area in the hydrogen underpotential deposition (H_{UPD}) region decreases with decreasing Pt surface sites available. Also an anodic shift in the reduction peak is observed for the two 30% Pt–Co/C alloys relative 30% Pt/C which can be attributed to a decrease in desorption free energy of Pt–OH, Pt–O or $Pt–O_2$ due to the presence of the alloying element implying that the reduction of oxygen containing intermediate species is more facile. It is also interesting to compare the H_{UPD} region for the two-supported Pt–Co catalysts. The shape of the H_{UPD} region for Pt_3Co (76% Pt) is very similar to that of Pt catalyst and shows typical hydrogen adsorption/desorption features in the potential range of 50–400 mV, whereas Pt_2Co (68% Pt) exists more in alloy form with poorly resolved H adsorption/desorption features.

Fig. 9 shows typical cyclic voltammograms of Pt–Co alloys in alkaline media using 1M KOH at 10 mV/s. The redox couple observed between 0 V and −0.2 V (versus Hg/HgO) is due to the redox processes involving metallic Co in alkaline medium leading to the formation of Co_3O_4 and/or CoOOH as indicated by Pourbaix diagram of Co and detailed electrochemical investigations [46]. Co oxidation peaks are not discernable due to large double layer current but the corresponding reduction peaks are evident. It is observed from these cyclic voltammograms that Pt_3Co shows higher Co redox peaks compared to that of Pt_2Co for the same loading of 14 $\mu g_{Pt}/cm^2$ on the glassy carbon disk. On the contrary, EDS measurement which is a bulk averaged technique, shows a cobalt composition of only 25% for Pt_3Co compared to that of 30% for Pt_2Co. This implies that in Pt_3Co more Co is present on the surface compared to Pt_2Co, in turn observed as higher metallic Co redox currents in Pt_3Co than Pt_2Co.

3.3. Oxygen reduction reaction (ORR) kinetics and peroxide yield measurement

Fig. 10 shows a representative set of rotating ring-disk experiments performed on Pt and Pt-alloy catalysts in O_2 saturated 1 M $HClO_4$ at room temperature using a constant Pt metal loading

Table 3
Electrokinetic parameters for the different electrocatalysts used in this study in 1 M $HClO_4$ at room temperature from RDE measurements at 900 rpm

Catalyst	i_k @ 0.9 V (mA/cm^2_{Pt})[a]	i_k @ 0.8 V (mA/cm^2_{Pt})	$i_o \times 10^9$ (A/cm^2_{Pt})[b]	Tafel Slope (mV/dec)[c]	ECA (m^2/g_{Pt})[d] [H_{UPD} region]
30% Pt/C	0.078	0.918	0.230	60/122	44
60% Pt/C	0.141	0.960	0.852	63/125.5	23
30% Pt_2Co/C	0.408	2.325	1.400	60/139	16
30% Pt_3Co/C	0.314	3.065	0.853	59.5/129	19

[a] i_k – kinetic current density.
[b] i_o – equilibrium exchange current density.
[c] Extracted from the anodic sweep of ORR from 0.35 V to 1.2 V vs. RHE.
[d] Based on 210 $\mu C/cm^2$ for atomic hydrogen oxidation on a smooth Pt surface.

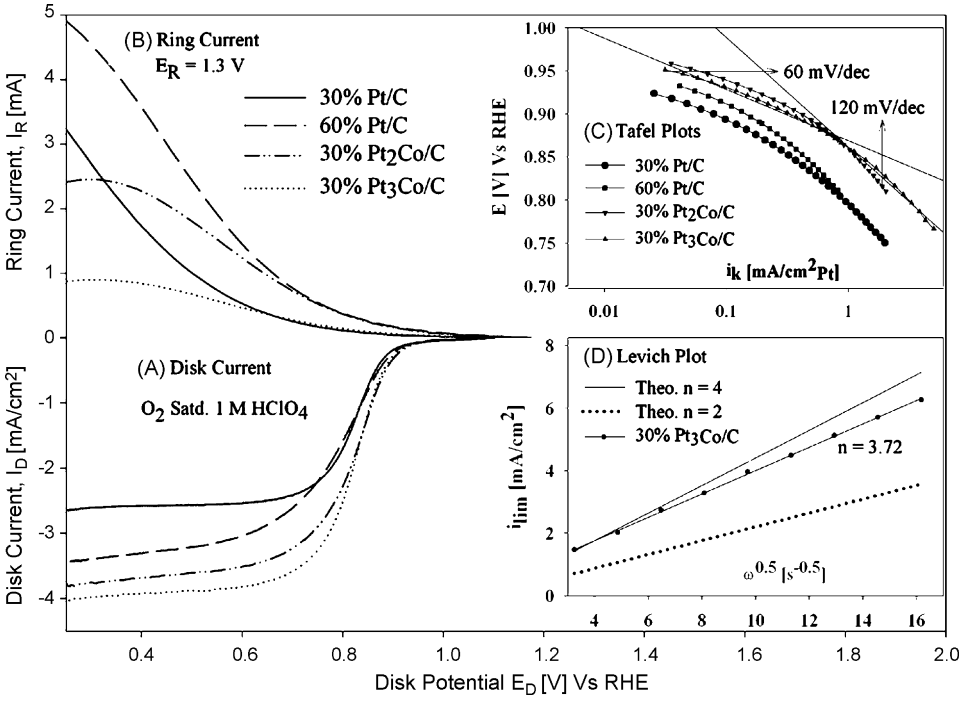

Fig. 10. Disk (A) and ring (B) currents obtained on 30% Pt/C, 60% Pt/C, 30% Pt_2Co/C, and 30% Pt_3Co/C during ORR in the anodic sweep at room temperature with 1 M $HClO_4$ electrolyte at a disk rotation rate of 900 rpm and scan rate of 20 mV/s using a glassy carbon disk of 5 mm diameter and ring collection efficiency of 39%. (C) Tafel plots for the ORR at room temperature extracted from anodic sweep at 20 mV/s, 900 rpm. (D) Representative Levich Plot for the ORR on 30% Pt/C at various potentials; current densities normalized to the electrochemical surface area of platinum on 5 mm glassy carbon disk unless otherwise indicated in the plot.

of 14 $\mu g_{Pt}/cm^2$ on the glassy carbon (GC) disk. The voltammograms measured at a scan rate of 20 mV/s, are shown for a rotation rate of 900 rpm. Representative scans shown in the bottom left-hand side of Fig. 10(A), represents the anodic sweep. The anodic sweep represents a true comparison of ORR activity as it is taken immediately after the corresponding cathodic sweep and hence represents ORR activity after removal of the oxide layer formed at or near open-circuit conditions. While it may be argued that this may not represent true fuel cell operating environment it does represent a more accurate picture of the reaction center (Pt site) activity for ORR. In the potential region of 0.9–0.7 V versus RHE, mixed kinetic-diffusion controlled currents are observed ensued by a well-defined diffusion limiting current beyond 0.6 V. For the same Pt loading of 14 $\mu g/cm^2$ on the GC disk, 30% Pt/C and 60% Pt/C exhibit essentially similar ORR activity in the mixed kinetic-diffusion controlled region followed by a significantly lower diffusion controlled current for 30% Pt/C as compared to 60% Pt/C which can be attributed to the increased thickness of the catalyst layer on the GC disk for 30% Pt/C relative to 60% Pt/C, since the supporting carbon determines oxygen diffusion through the porous catalyst loaded on the GC disk. An exactly similar argument can also be extended to the two supported Pt–Co alloys with different Pt compositions, such that 30% Pt_3Co/C has a smaller catalyst layer thickness and hence higher diffusion limited current relative to 30% Pt_2Co/C. On comparing the Pt/C catalysts with Pt–Co/C alloy catalysts, it is seen that the two Pt–Co/C catalysts exhibit an anodic shift of about 30 mV in the mixed kinetic-diffusion potential region and hence 30 mV lower over potential for ORR. This lower overpotential of the alloy catalysts towards ORR is due to the fact that the presence of alloying element decreases the desorption free energy (ΔG_{des}) of Pt–OH, Pt–O or $Pt–O_2$ such that the adsorption of oxygen containing intermediate species on Pt surface sites is inhibited in the supported alloy catalysts compared to Pt/C [47]. This discussion based on the ORR profile for each catalyst involves interference from diffusion limited current densities i_{lim}, and hence Tafel plots are extracted using the following Eq. (1) by eliminating i_{lim} and obtaining a clearer picture based on kinetic currents.

$$i_k = \frac{(i_{lim}{}^{\bullet} i)}{(i_{lim} - i)} \quad (1)$$

where i_k is the kinetic current density, i is the measured current density during oxygen reduction polarization, and i_{lim} is the diffusion limited current density. Fig. 10(C) shows the corresponding Tafel plots of the Pt and Pt-alloy catalysts where the kinetic current densities are normalized on the basis of the electrochemical surface area of Pt. Firstly, it is noted that the activity of Pt-alloy catalysts are better than the Pt/C catalysts due to the unique effect of the surface Co species enabling lower oxide formation on Pt [48,49]. Taking into consideration that the initial adsorption of molecular oxygen on Pt is part of the rate-determining step (rds) [26], the coverage of oxides at or near the open-circuit potentials represents a surface poison. Hence, preferential oxide formation on surface Co as shown earlier is attributed to freeing Pt sites for initiating ORR [50]. However, the comparison of the relatively oxide free anodic scans exhibiting enhanced ORR is significant. This shows the concomitant oxide formation on Pt sites in the supported Pt–Co electrocatalysts is significantly

lower than the corresponding Pt/C catalysts (both 30% and 60% on carbon loading). This in the background of previous observations of experimentally derived activation energies on these class of supported catalysts and agreement with theoretical calculations on transition states [51] indicates that the observed enhancement is direct effect of surface oxide coverage. Also, it is seen from the Tafel plot that the Tafel slope is constantly changing, which is due to the continuously varying charge transfer coefficient (α) value from 0 to 1 with overpotential; however, it is possible as a gross approximation to obtain Tafel slope (Table 3) representing two distinct regions, in good comparison with previously reported literature values [52], yielding two different Tafel slopes of $-2.3RT/F$, i.e., 60 mV/decade at low overpotentials ($E > 0.85$ V) and $-2(2.3RT/F)$, i.e., 120 mV/decade at high overpotentials ($E < 0.85$ V) which agree very well with prior reports on single-crystal Pt electrodes [53], carbon-supported Pt [54] and pc-Pt plug [26]. This change from 60 mV/decade to 120 mV/decade is closely related to earlier contention of the adsorbed OH species at potentials beyond 0.85 V versus RHE corresponding to 60 mV/decade of Tafel slope, where as at higher overpotentials, 120 mV/decade indicates a clean catalytic surface devoid of any oxygen containing adsorbed intermediate species that can affect the adsorption of molecular O_2 from the solution to the active surface site for subsequent reduction [26]. Cyclic voltammogram measured in alkaline electrolyte shown in Fig. 9 as explained earlier indicate that the Pt_3Co/C surface is rich with cobalt which can inhibit the adsorption of oxygenated intermediate species on the Pt surface sites thereby avoiding H_2O_2 generation pathways and providing a direct route for H_2O formation. Subsequently, ring current (also peroxide yield values shown in Table 3) of Pt_3Co catalyst imply a very low amount of peroxide generation presumably attributed to the rich cobalt on the surface.

Fig. 10(D) shows the representative Levich plot for 30% Pt_3Co/C used in this study at various rotation rates from 100 rpm to 2500 rpm. Similar plots were obtained with the other three catalysts and hence not shown here. Levich plot yields the so called Levich constant B, according to relation (2) [55] given below for ORR limiting current i_{lim}, from which the number of electrons transferred was calculated to be 3.72 for Pt_3Co indicating a predominant four-electron transfer.

$$i_{lim} = B\omega^{1/2} \tag{2}$$

where $B = 0.62nFD^{2/3}\nu^{-1/6}C$, where n is the number of electrons transferred, F is the Faradays Constant, D is the diffusion coefficient of O_2 in the electrolyte, C_o is the oxygen concentration in the electrolyte, ν is the kinematic viscosity and ω is the rotation rate in rpm.

Hydrogen peroxide yield due to the parallel pathway for ORR was also analyzed by classical rotating ring-disk electrode (RRDE) technique. The formation of relative amount of H_2O_2 and H_2O can be determined quantitatively with the RRDE experiment by holding the potential of the ring at 1.3 V versus RHE, where H_2O_2 formed at the disk during oxygen reduction is readily oxidized at the ring. Fig. 10(B) shows the currents measured at the ring during the anodic sweep of the disk potential shown in figure at room temperature in 1M $HClO_4$ at 900 rpm. Table 4 shows the comparison of peroxide yields measured at the gold ring when the corresponding disk electrode potentials were 0.4 V, 0.6 V and 0.7 V versus RHE and calculated using the following relation,

Table 4
Peroxide yields (mole fraction) measured using a RRDE technique with a rotation rate of 900 rpm and various disk potentials of 0.7 V, 0.6 V, 0.4 V vs. RHE in conjunction with a gold ring electrode polarized at 1.3 V in 1M $HClO_4$ at room temperature

Catalyst	$\%H_2O_2$ @0.7 V	$\%H_2O_2$ @0.6 V	$\%H_2O_2$ @0.4 V
30% Pt/C	0.111	0.257	2.330
60% Pt/C	0.394	0.753	2.408
Pt_2Co/C	0.342	0.652	3.523
Pt_3Co/C	0.160	0.260	0.510

$$\chi_{H_2O_2} = \frac{2(I_R/N)}{(I_D + (I_R/N)} \tag{3}$$

where N is the collection efficiency of the ring, χ is the mole fraction of peroxide formed, I_D and I_R are the disk and ring currents, taking into account the total disk currents for the oxygen reduction as the sum of reduction currents of O_2 to H_2O and H_2O_2 and the collection efficiency N for the ring electrode [26].

These data in Table 4 are an indication of potential dependence of peroxide yield at disk electrode for the various catalysts used in these experiments. Peroxide currents are negligible for disk potentials above 0.65 V indicating that oxygen reduction predominantly proceeds via four-electron transfer process without significant peroxide generation, which is relevant for the operating potential of fuel cell cathodes. This is the region where the cathode potential of a normal operating fuel cell lies, and alludes to the importance of maintaining a stable cell potential with regard to the interfacial stability of the MEA, especially in the case of discontinuous fuel cell operation in which considerable voltage fluctuations take place frequently. Below the normal fuel cell operating potential of 0.6–0.7 V versus RHE, peroxide generation begins to increase significantly followed by much higher ring currents at a diffusion controlled disk potential of 0.4 V. This potential dependence of peroxide yield is correlated to fuel cell membrane degradation in the next section. It is also observed that as the disk potential further extends into the H_{UPD} region, the ring currents of the two Pt/C samples keeps increasing. In the case of the Pt/C catalysts, as the disk potential enters H_{UPD} region enhanced peroxide generation occurs as H_{UPD} blocks the Pt surface sites necessary to split the O_2 molecule leading to increased peroxide generation. This is important in cases where H_2 permeation from the anode feed to the cathode catalyst through the membrane is significant as this is also a possible pathway of peroxide generation and subsequent membrane degradation.

3.4. Assignment of the absorption bands of ATR-IR Spectra of Nafion® 112 (H-form)

Infrared absorption studies, along with small angle X-ray, neutron scattering investigation and scanning probe microscopy

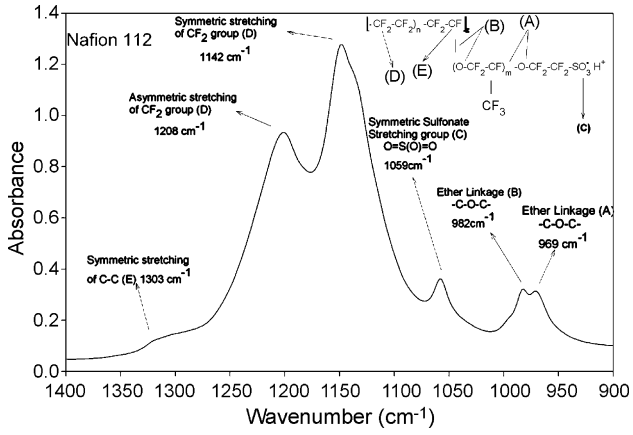

Fig. 11. ATR-FTIR spectrum of Nafion®112 (H-form) indicating absorption bands obtained using ZnSe ATR crystal. [See text for references].

imaging, have been used widely to elucidate the nanostructure of Nafion® membrane. Fig. 11 and Table 5 indicates the assignment of various vibrational absorption bands [40,41,56–59], in the region between 900 cm^{-1} and 1350 cm^{-1} wavenumbers as relevant to this study, associated with the chemical structure of Nafion®112 membranes (DuPont Corp.) in H-form shown in Fig. 1. The very strong absorption bands at 1142 cm^{-1} and 1208 cm^{-1} wavenumbers correspond to the symmetric and asymmetric vibrations of $–CF_2$ groups in the hydrophobic fluorocarbon backbone, symmetric stretching of the sulfonate group is observed at 1059 cm^{-1}. The twin peak at 969 cm^{-1} and 982 cm^{-1} is due to the presence of two ether linkages (–C–O–C–) in Nafion® side chain. Of the two ether vibrational absorption bands in Nafion® membrane, the higher frequency band (i.e., the one at 982 cm^{-1}) is attributed to the ether linkage directly attached to the fluorocarbon backbone and is labeled as ether band 'B'. Further the corresponding lower frequency component at 969 cm^{-1} is labeled as ether band 'A', caused due to its proximity to the sulfonate group and its electron withdrawing character. This assignment of vibrational absorption bands of ether linkages is due to the work done by Cable et al. [56], who contrasted the two ether absorption peaks in Nafion® against a single ether absorption band present in Dow perflourosulfonate ionomers (PFSI). Dow PFSI has only one ether linkage in its side chain and exhibits a single absorption peak centered at around ~969 cm^{-1}.

Hsu et al. [60], proposed the ion-cluster network theory for the morphology of Nafion® membranes according to which sulfonate groups with terminating pendant side chains stretch out into approximately spherical clusters also consisting of water and hydrated cations, interconnected to each other by channels for ionic transport, and supported by hydrophobic fluorocarbon backbone material. Meanwhile, Yeager and Steck [61] corroborated the conclusions of Falk [62] (that the ionic clusters are non-spherical in shape and have intrusions of side chain ether linkages), by proposing three-phase morphology for Nafion® consisting of the hydrophobic fluorocarbon phase, hydrophilic ionic clusters and an interfacial region between these two. This interfacial region is largely a void volume containing pendant side chain materials, a small amount of sorbed water and trace level of sulfonate exchange sites and counter-ions. From the results of this present study, this interfacial region is of importance since they turn out to be the vulnerable site for radical species attack during fuel cell operation as discussed in the following sections.

Table 5
Selective list of IR absorption peak assignments of H-Nafion® 112 as pertinent to this study in correspondence with Fig. 2

Index	Wavenumber[a] (cm^{-1})	Peak assignments
(A)	969 m	υ_s(C–O–C), ether band 'A', symmetric
(B)	982 m	υ_s(C–O–C), ether band 'B', symmetric
(C)	1059 m	υ_s (SO_3^-), sulfonate group, symmetric
(D)	1142 vs	υ_s (CF_2), CF_2 group, symmetric
(D)	1208 vs vb	υ_{as} (CF_2), CF_2 group, asymmetric
(E)	1303 sh	υ_s (C–C), symmetric

[a] Relative intensity: m – medium; vs – very strong; vb – very broad; sh – shoulder.

3.5. *Effect of radical-initiated degradation on membrane properties*

Segmented cell durability tests were conducted to investigate the mechanism of degradation as a function of potential, temperature, choice of electrocatalyst, catalyst loading, and test duration. Cathode operating potentials of 0.4 V, 0.6 V and 0.7 V versus RHE were employed to study the influence of peroxide yield, subsequent membrane deterioration and also to correlate segmented cell durability test results to RRDE data discussed above. Tests were conducted at room temperature, 40 °C, 60 °C, and 80 °C to study the influence of temperature for various time scales of 24 or 48 h. At the end of each durability test, the membrane was carefully separated from the electrode; the changes in its proton conductivity (σ), ion exchange capacity (η) were

Table 6
Effect of cathode-side durability tests with O_2/N_2, 40 °C, 1 atm, for a duration of 24 h using 30% Pt/C, 60% Pt/C, 30% Pt_2Co, 30% Pt_3Co at two different working electrode (WE) polarization potentials of 0.4 V and 0.6 V vs. DHE

Catalysts	WE @ 0.4 V		WE @ 0.6 V	
	$\frac{\sigma_{after}-\sigma_{before}}{\sigma_{before}}$ (%)	$\frac{\eta_{after}-\eta_{before}}{\eta_{before}}$ (%)	$\frac{\sigma_{after}-\sigma_{before}}{\sigma_{before}}$ (%)	$\frac{\eta_{after}-\eta_{before}}{\eta_{before}}$ (%)
30% Pt/C	34	26	27	19
60% Pt/C	57	48	49	43
30% Pt_2Co/C	50	40	44	34
30% Pt_3Co/C	27	22	16	9

Listed are the decreases in proton conductivity σ (S/cm) and ion exchange capacity η (mEq/g).

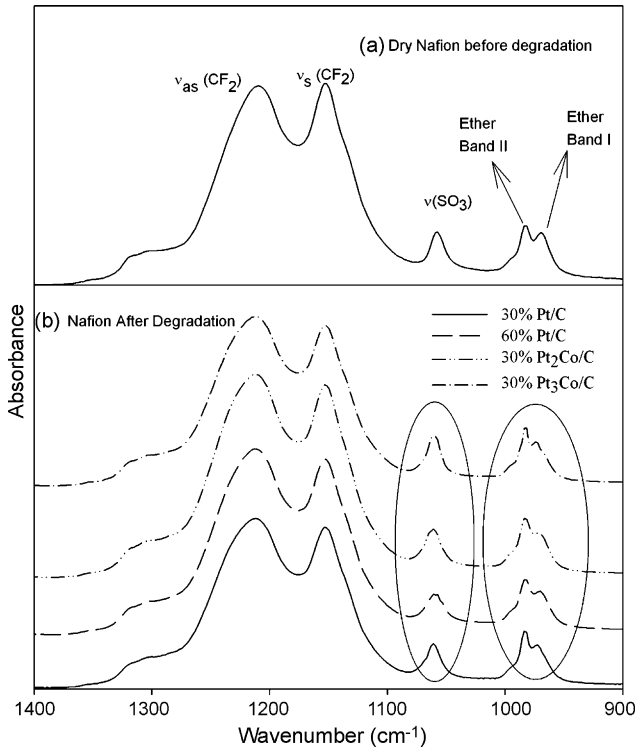

Fig. 12. ATR-FTIR Spectrums of Nafion® obtained using Ge ATR crystal before and after cathode-side degradation tests with four parallel samples as indicated in the plot, operated for 24 h at 0.4 V (WE vs. DHE), 40 °C cell temperature and 1 atm pressure conditions. (a) IR Spectrum (900–1400 cm^{-1}) before degradation. (b) IR Spectrum after degradation.

determined and compared with that of the non-degraded pure Nafion® membrane properties shown in Table 1, to estimate the extent of degradation quantitatively; ATR-IR absorption spectra of degraded membranes were compared to spectra of pristine membrane (Fig. 11) to determine the site of membrane degradation.

Table 6 shows the results of cathode-side degradation tests conducted at 0.4 V and 0.6 V (WE versus DHE), 40 °C, 1 atm pressure conditions for duration of 24 h with four parallel electrocatalysts 30%Pt/C, 60%Pt/C, 30%Pt_2Co and 30%Pt_3Co. Fig. 12 compares the FTIR spectrums of the Nafion® membranes before and after degradation test at 0.4 V, 40 °C, 1 atm pressure conditions for duration of 24 h using Ge crystal with IR penetration depth of 0.65–0.7 μm. The most significant difference after this 24 h test is observed at the ether band 'A' peak at 969 cm^{-1} as a decrease in its intensity of absorption. There is a concomitant effect of cleavage of ether band 'A' and the relatively small decrease in intensity of sulfonate vibrational band at 1059 cm^{-1}, and the reason for this is discussed below. Vibrational absorption peak at 969 cm^{-1}, as discussed earlier in this article, is due to the ether bond present closer to the sulfonate ion exchange site in the pendant side chain. The vibrational ether band 'B' at 982 cm^{-1}, due to the ether linkage directly attached to the fluorocarbon backbone is relatively unaffected compared to the band at 969 cm^{-1}, indicating a preferential cleavage of the ether linkage directly attached to the sulfonate exchange groups. Quantitative results from IR absorbance plot of the membrane can be obtained only if an internal reference is incorporated in the membrane that does not degrade during the durability test [63]. Since such an internal reference might interfere with durability testing, it was not preferred in this study. For the purpose of semi-quantitative comparison the concept of relative absorbance has been used here. For example, with the 30% Pt/C catalyst sample, ratio of absorbance intensity of ether band 'A' to the symmetric –CF_2 stretching peak ($H\upsilon_{(-C-O-C-)I}/H\upsilon_{(-CF_2)}$) decreased to 0.256 (after test) as compared to the initial ratio of ($H\upsilon_{(-C-O-C-)I}/H\upsilon_{(-CF_2)} = 0.312$. –$CF_2$ symmetric stretching peak is used as the reference peak for normalization since it did not decrease in intensity during the course of the experiment. It is noted here that the spectra in Fig. 12 is obtained using Ge ATR crystal that provides a penetration depth of only 0.65–0.7 μm and same test performed with ZnSe ATR crystal (penetration depth 1.7–2 μm) did not exhibit any significant decrease in any of the IR absorption bands indicating that this cleavage is highly localized on the surface and has not probably affected the membrane beyond a distance of ∼1 μm from the surface. Table 7 shows the decrease in relative intensity of ether band A in Nafion®112 after cathode-side durability test at the indicated conditions with the four Pt and Pt-alloy catalysts. Further, the decrease in intensity of ether band 'B' ($H\upsilon_{(-C-O-C-)II}/H\upsilon_{(-CF_2)}$) was negligible and not shown here. Subsequently, loss in conductivity and IEC shown in Table 6 is also due to the preferential cleavage of ether band 'A' in the side chain, because this cleavage scissions off the sulfonate ion exchange sites present at the terminal end of the pendant side chain and directly attached to ether band 'A'. Also a very minor shift in the vibrational frequency of the sulfonate exchange sites to higher values is observed. Vibrational stretching frequency of sulfonate group $\upsilon_s(SO_3)$ in pure Nafion®-H form is localized in the spectral region around 1059 cm^{-1}. $\upsilon_s(SO_3)$ of the degraded membranes is observed around 1062–1064 cm^{-1} and this is due to the modest contamination of membrane by counter ions (such as Na^+, Rb^+, Li^+, Cs^+, Ca^+), because minor cationic impurities

Table 7
Percentage decrease in intensity of IR absorption of ether band 1 at 969 cm^{-1} and sulfonate symmetric stretching bang at 1059 cm^{-1} after cathode-side degradation test performed at 40 °C, ambient pressure, for a duration of 24 h at a WE potential of 0.4 V vs. DHE

Catalyst	% A_{ratio} $\nu_{(C-O-C)\,I}$	% A_{ratio} $\nu_{(SO_3)}$	H_2O_2 yield @ 0.4 V (%)[a]
30% Pt/C	18 %	22%	2.330
60% Pt/C	39%	37%	2.408
30%Pt2Co/C	21%	23%	3.523
30%Pt3Co/C	12%	13%	0.510

$A_{ratio}[\nu(C-O-C)I] = (H\upsilon_{(-C-O-C-)I}/H\upsilon(-CF_2))$ and $A_{ratio}[\nu(SO_3)] = (H\upsilon_{(SO_3)}/H\upsilon_{(-CF_2)})$. % $A_{ratio} = (A_{ratio(before)} - A_{ratio(after)})/A_{ratio(before)}$.
[a] H_2O_2 obtained from ring current using Eq. (3).

from the carbon support, gas diffusion electrodes, humidification bottles, other fuel cell hardware are inevitable in the fuel cell operation. These foreign cations, usually have stronger affinity with the sulfonic acid group compared to H^+, and thereby replace the protons (H^+) attached to the sulfonate ion exchange sites; this replacement of protons by metal impurities causes a polarization of S–O dipoles and subsequently shifts $\upsilon_s(SO_3)$ to higher frequencies [40,56,64]. Also IEC indicated in Table 6 suffers a loss similar to the decrease in conductivity due to the loss of ion exchange sites. A comparison between peroxide yield in Table 4 for the various catalysts, loss in conductivity and IEC in Table 6 and decrease in ratio of absorbance in Table 7 indicates a direct one-on-one relationship between peroxide yields obtained on the ring electrode and membrane degradation. 60% Pt/C and 30% Pt_2Co/C catalysts exhibited significantly higher peroxide yield on the ring at all potentials below 0.7 V versus RHE and is reflected in the high levels of degradation observed in membrane characteristics in the durability experiment. Further, 30% Pt_3Co/C that consistently yielded low peroxide on the ring at all potentials gives rise to a low level of loss in membrane properties after cathode-side durability testing. This clearly indicates that the degradation on the cathode side is most likely due to peroxide radicals generated from local interfacial Fenton type catalysis of H_2O_2 in turn generated from the $2e^-$ pathway of ORR.

Fig. 13 shows the IR plot of degraded membranes in the spectral region 1100 cm^{-1} to 940 cm^{-1} after cathode-side degradation test performed at 40 °C, 1 atm pressure conditions for duration of 24 h using three parallel samples of 30% Pt/C as the cathode catalyst at various cathode operating potentials of 0.4 V, 0.6 V, 0.7 V versus DHE. At normal cathode operating potentials of 0.6 V and 0.7 V the cleavage of ether band 'A' is relatively less intense than at an accelerated cathode operating potential of 0.4 V, due to significantly higher peroxide formation at 0.4 V. Potential dependent cleavage of ether band 'A' shows that the peroxide radical generation at various operating fuel cell potential is directly correlated to the subsequent polymer membrane.

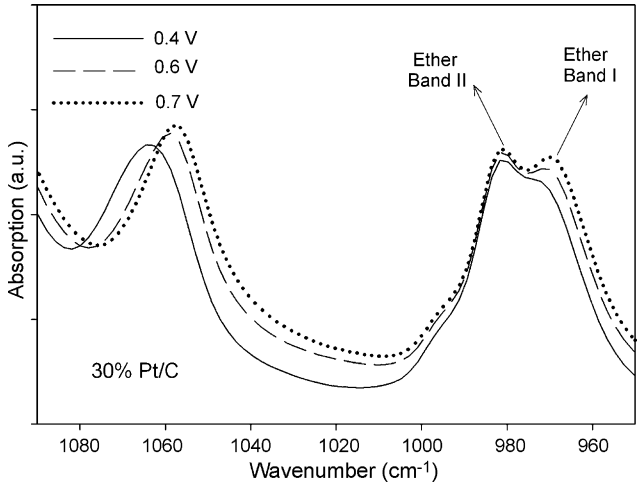

Fig. 13. Potential dependent cleavage of ether band 'A'. Shown are the IR Spectra of Nafion® after cathode-side degradation test at 40 °C, 1 atm pressure conditions for a duration of 24 h using 30% Pt/C catalyst.

Table 8
Loss in conductivity and peroxide yield from 30% Pt/C after cathode-side degradation test at 40 °C, ambient pressure, for 24 h at various WE potentials of 0.4 V, 0.6 V, 0.7 V vs. RHE

	WE@ 0.7 V	WE @ 0.6 V	WE @ 0.4 V
Peroxide yield (%)	0.111	0.257	2.330
Loss in conductivity (%)	16%	27%	34%

It is also seen that the intensity of ether band 'B' is relatively unaffected during the durability test.

As discussed above, the small decrease in intensity of $\upsilon(SO_3)$, shown in Table 8, attributed to cleavage of ether band 'A' results in the scission of the sulfonate group present at the terminal end of the pendant chain. Fig. 2 shows the vulnerable region for radical attack based on the result of this study. It is also seen that 60% Pt/C which has higher catalyst loading and higher particle size (Table 2) as compared to 30% Pt/C gives higher peroxide yield observed from RRDE results (Fig. 10) and correspondingly higher loss in membrane conductivity (Table 6) from durability testing.

As shown in Fig. 1, based on the chemical structure of Nafion®, the repeating unit of the fluorocarbon backbone, characterized by the value '*m*', determines the dry weight of the membrane and also its ion exchange capacity [41,59] (number of moles of sulfonic acid ion exchange sites per gram of dry polymer membrane) which varies from 0.55 mEq/g to 1.05 mEq/g. Ion exchange capacity (IEC) of the degraded membranes, as shown in Table 6, shows a loss similar to that of the proton conductivity. Since the vibrational absorption bands at 1142 cm^{-1} and 1208 cm^{-1} represent the fluorocarbon backbone ($–CF_2$ groups), the relative intensity of absorption is determined by the factor '*m*'. This remains unaffected after 24 h of cathode-side degradation test performed at 0.4 V versus DHE for the four cathode catalysts used in these experiments, thus the decrease in IEC can be attributed directly to the loss of sulfonate exchange sites. Decrease in proton conductivity and IEC values followed by relative decrease in IR intensity of one of the ether bands and no decrease in fluorocarbon backbone IR absorption signature implies that the radical species do not attacked the fluorine groups of the hydrophobic backbone.

Following the discussions of Falk [62] and Cable et al. [56] regarding the chemical nanostructure of Nafion® membrane briefly summarized above, it is likely that part of the side chain ether linkage intrudes into the hydrophilic ionic clusters. Consequently, during this period of 24 h of cathode-side degradation tests, it is observed that the radical species generated during the course of fuel cell operation initiates the polymer chain breakage by attacking the hydrophilic ionic cluster region (specifically the ether linkage intruding into the hydrophilic ionic cluster region) and virtually does not degrade the hydrophobic backbone of the membrane.

In order to understand the prolonged effect of fuel cell operation on membrane durability, cathode-side degradation test was also performed for a period of 48 h at various operating potentials, and temperature conditions. Table 9 shows the results of a 48 h cathode-side degradation test performed at 40 °C, 1 atm

Table 9
Effect of cathode-side durability tests with O_2/N_2, at 40 °C, 1 atm, for a duration of 48 h using 30% Pt/C, 60% Pt/C, 30% Pt_2Co, 30% Pt_3Co at a polarization potential of 0.4 V vs. DHE

Catalysts	$\frac{\sigma_{after}-\sigma_{before}}{\sigma_{before}}$ (%)	$\frac{\eta_{after}-\eta_{before}}{\eta_{before}}$ (%)
30% Pt/C	44	27
60% Pt/C	73	44
30% Pt_2Co/C	74	38
30% Pt_3Co/C	51	24

Listed are the percentage decrease in proton conductivity σ (S/cm) and ion exchange capacity η (mEq/g).

pressure conditions, and 0.4 V versus DHE cathode operating potential simultaneously using four parallel electrodes containing catalysts, 30% Pt/C, 60% Pt/C, 30% Pt_2Co, 30% Pt_3Co. Table 9 indicates the decrease in proton conductivity values remain linear with time. Further the relative changes in conductivity reflect previous correlation with peroxide yields. However surprisingly, the corresponding linear decrease in IEC values is not observed. An apparent stabilization occurs after the initial decrease in the first 24 h. Corresponding IR plots of degraded membranes after 48 h shown in Fig. 12 exhibit a significant decrease in absorption bands at 1142 cm^{-1} and 1208 cm^{-1} attributed to the hydrophobic fluorocarbon backbone reflecting that the membrane backbone has undergone degradation. The fact that IEC capacity does not decrease linearly after this prolonged test appears to be due to the simultaneous loss of sulfonate exchange sites concurrent with loss of fluorocarbon groups from the membrane backbone. This leads to a decrease in the dry membrane weight in such a way that IEC (number of moles of sulfonic acid ion exchange sites per gram of dry polymer membrane) does not change. Insets (a) and (b) in Fig. 14 shows the decrease in intensity of the ether linkages and sulfonate symmetric bands. Also the sulfonate stretching bands are shifted to higher wavenumbers due to modest contamination

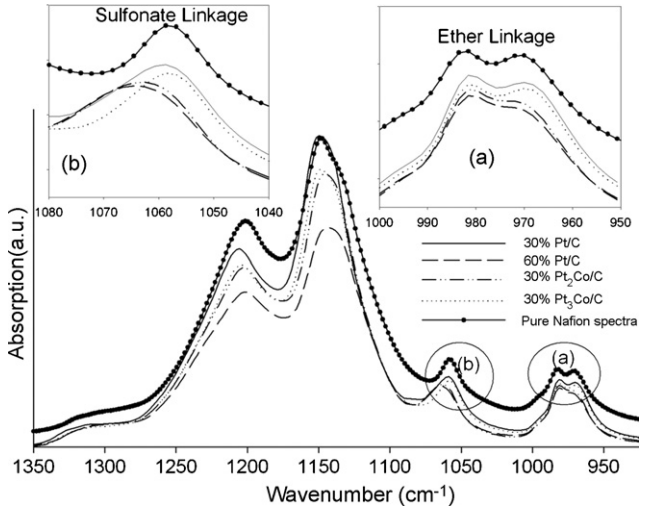

Fig. 14. ATR-FTIR Spectra of Nafion® after cathode-side degradation tests with four parallel samples as indicated in the figure, operated for 48 h at 0.4 V (WE vs. DHE), 1 atm pressure and 40 °C temperature conditions obtained from ZnSe ATR crystal. Also shown are magnified views of the ether linkages [Inset (a)] and sulfonate symmetric stretching peaks [Inset (b)].

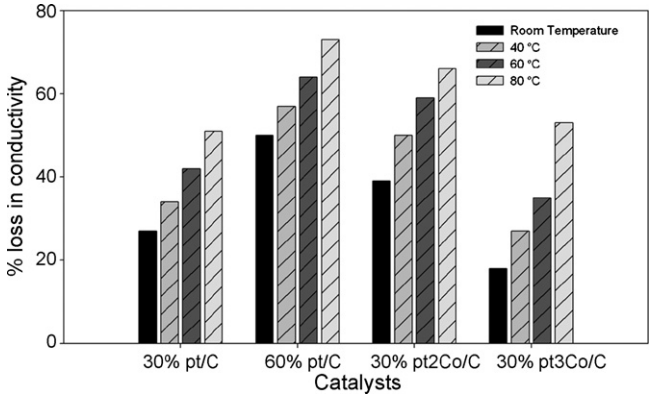

Fig. 15. Temperature dependence of conductivity after cathode-side degradation test with four parallel catalysts 30% Pt/C, 60% Pt/C, 30% Pt_2Co/C and 30% Pt_3Co/C at 0.4 V at ambient pressure and various temperatures.

in the form of cationic impurities that replace the protons in the membrane as already discussed earlier in this article. This indicates that the membrane degradation due to radical species generated during the course of fuel cell operation is initiated by cleavage of certain sections of ether band 'A' intruding into the hydrophilic ionic clusters and then later spreads to the hydrophobic fluorocarbon backbone thereby slowly degrading the bulk of the membrane.

Fig. 15 shows the loss in proton conductivity for the four catalysts after cathode-side degradation performed for 24 h at ambient pressure and 0.4 V versus DHE as a function of temperature in the range starting from room temperature (RT) to 80 °C.

Similar behavior was observed with IEC data and not shown here. It is seen that as the temperature increases there is an increase in loss of conductivity, however the differential change in conductivity loss with temperature is not very high, it implies that at higher temperatures, despite higher overall ORR current densities obtained, the current due to H_2O_2 formation as a fraction of H_2O formed remains approximately the same.

Previous results using data of membrane degradation after exposure to Fenton's solutions such as those reported by Inaba [65] concluded that both main chain and side chains are decomposed at similar rates by radical attack. However, their experimental results bear no relation to electrochemical environment of an operating fuel cell. In addition, there is no direct correlation with cathode or anode interface. By contrast our fuel cell setup shows that the hydrophilic regions within the membrane structure are more prone to radical species attack in the initial stage of fuel cell operation followed by decomposition of the hydrophobic main chains during prolonged exposure to these accelerated degradation conditions. Previous study [13,18] have shown that SO_2 and CO_2 were observed in the outlet stream of an operating fuel cell which is presumably due to the loss of ether linkage and sulfonate groups from the membrane side chain and terminal groups, respectively. In the literature, fluoride emission rate (FER) has been frequently used as a measure of Nafion® membrane degradation, but such studies were not done here because in our segmented cell experimental setup four parallel samples run simultaneously with a common outlet for the

Table 10
Effect of anode-side durability with O_2/H_2 for 48 h at 1 atm pressure as a function of temperature (60 °C and 80 °C), polarization potential (OCV, 0.1 V), and choice of anode electrocatalysts (30% Pt/C, 60% Pt/C)

Catalyst	T (°C)	WE potential	$\frac{\sigma_{after}-\sigma_{before}}{\sigma_{before}}$ (%)	$\frac{\eta_{after}-\eta_{before}}{\eta_{before}}$ (%)
30% Pt/C	60	OCV	–	–
		0.1 V	2	4
	80	OCV	2	3
		0.1 V	3	3
60% Pt/C	60	OCV	4	4
		0.1 V	5	6
	80	OCV	3	7
		0.1 V	4	10

Listed are the decreases in proton conductivity σ (S/cm) and ion exchange capacity η (mEq/g) of Nafion® 112 membrane.

gas stream and fluoride ions detected at the outlet stream represents a total loss from the membrane due the combined effect of the four samples. Further, the fluoride release represents the extent of the polymer degradation without any detailed information on the nature of attack and the regions of the membrane undergoing degradation at any given operating condition.

3.6. Anode-side durability tests

As explained in the experimental section, anode-side durability test involved the passage of H_2 over catalyzed anode and O_2 over non-catalyzed gas diffusion layer (GDL) in order to investigate membrane degradation on the anode side due to O_2 permeation through the membrane. In this test only 30% Pt/C and 60% Pt/C catalysts were chosen for anode-side durability tests since the Pt–Co/C alloys are cathode relevant catalysts. The membrane samples were obtained after subjecting them to two types of conditions: (i) holding the potential of the working electrode in the MEA at possible anode electrode overpotential of 0.1 V for 48 h and (ii) in open-circuit voltage (OCV) condition for 48 h. Table 10 shows the decrease in proton conductivity and ion exchange capacity after anode-side durability tests performed at 60 °C and 80 °C at OCV and 0.1 V versus RHE. Decreases in conductivity and ion exchange capacity are significantly lower than those observed in the cathode-side tests as shown in Table 10 after this 48 h test indicating that for the duration of the experiment performed there is no significant degradation on the anode side. This result is not surprising since the O_2 permeation rate through Nafion® 112 membrane is relatively low and our previous study on hydrocarbon membranes such as sulfonated poly ether sulfone (SPES) and Nafion 1135 indicate similar low level of degradation on the anode side [4]. Also considering the fact that in this experiment the non-catalyzed GDL on the cathode side does not consume O_2, as a result the test is specific to probing the interaction of adsorbed hydrogen on a working catalyzed GDL and the effect of crossover oxygen. A separate test wherein hydrogen oxidation occurs in significant rate (higher current density) in the same O_2 crossover environment is a case for future work. In a prior long-term fuel cell performance study on radiation-grafted-FEP-g-polystyrene-type membranes, Buchi et al. [15] reported that the rate of radical-initiated degradation increases with increasing gas crossover. They also claimed that gas crossover is a prominent factor for the degradation process, especially under OCV conditions; however, whether oxygen or hydrogen crossover is the predominant contributor could not be ascertained in their regular fuel cell setup. In our case, the suspected formation of radicals due to hydrogen crossover to the cathode side may be eliminated as a source of peroxides at the cathode, because no Pt reaction sites were present in the O_2 side of our experimental setup (non-catalyzed GDL). It has also been shown earlier that degradation of membrane due to either H_2 crossover to the cathode and/or O_2 crossover to the anode side result in only less than 3% loss in efficiency due to slower diffusion rates of these gases through the membrane [13]. Also Liu et al. [31] showed that for short periods of durability tests, H_2 crossover to the cathode side is very minimal and thereby ruling out the possibility of significant degradation of the membrane at the anode side. Finally, regarding the anode-side durability tests the present results cannot rule out the possible occurrence of radical catalyzed membrane degradation at the anode side when anode side is subject to higher current density (hydrogen oxidation conditions) in longer testing periods and it is here found that the rate of degradation on the cathode side is much higher than that on the anode side under the accelerated conditions used in this study.

4. Conclusions

Novel accelerated technique was used to investigate and correlate the peroxide generation at an electrode/electrolyte interface from the perspective of radical-initiated perfluorinated membrane degradation as a function of choice of electrocatalyst, catalyst loading on carbon support, operating overpotential, temperature, and presence of alloying element on the surface against Pt rich outer layer. Membrane degradation process was also separately studied in half-cell configurations so that the two formerly proposed PEM degradation mechanisms could be evaluated individually without interference. Peroxide generation observed on the ring electrode of a RRDE for various electrocatalysts used in this study showed a one-on-one relation with the level of degradation of perfluorinated membrane via local Fenton type reactions at the cathode-membrane interface of an operating fuel cell due to the simultaneous $2e^-$ pathway of ORR along with the more predominant $4e^-$ reduction to water. Cleavage of the side chain ether linkage, which intrudes into the hydrophilic ionic cluster, is found to be the key initiator of conductivity and ion exchange capacity loss. Prolonged durability testing leads to breakage of certain sections of fluorocarbon backbone as observed in the stabilization of ion exchange capacity versus a more linear decline in proton conductivity. Normal operating cathode overpotentials of 0.6 V and 0.7 V versus DHE leads to lower membrane degradation relative to higher overpotentials of 0.4 V, this is directly correlated to peroxide yields observed independently during RRDE measurements. Higher the loading of catalyst on carbon support and corresponding larger the particle size results in higher peroxide yield and consequent higher membrane degradation as shown by the comparison between

60% Pt/C and 30% Pt/C used in this study. Pt–Co/C alloy catalyst with enrichment of surface Co gives lower peroxide current and maintains lower level of membrane degradation as shown by the comparison between Pt_2Co/C and Pt_3Co/C. Temperature effects on membrane degradation was found to be linear with higher ORR activity and consequent higher peroxide generation at the interface. Degradation at the anode side due to oxygen crossover through the membrane was found to be insignificant relative to cathode-side degradation within the duration of the experiments performed here. However, these tests represent the narrow confines of interaction of absorbed hydrogen on Pt and its interaction with crossover oxygen.

Acknowledgments

The authors deeply appreciate the financial assistance of the Army Research Office under a single investigator grant. The authors also gratefully acknowledge the supply of electrocatalysts from BASF-fuel cells (Somerset, NJ, USA). Assistance from Dr. Freemen Chen (NU) during IR measurements and analysis for membrane samples is acknowledged.

References

[1] J. Xie, D.L. Wood III, D.M. Wayne, T.A. Zawodzinski, P. Atanassov, R.L. Borup, J. Electrochem. Soc. 152 (2005) A104.
[2] A.E. Steck, New materials for fuel cell systems I, Proceedings of the 1st International Symposium on New Materials for Fuel Cell Systems, Montreal, 1995, pp. 74–94.
[3] R. Baldwin, M. Pham, A. Leonida, J. McElroy, T. Nalette, J. Power Sources 29 (1990) 399.
[4] L. Zhang, S. Mukerjee, J. Electrochem. Soc. 153 (2006) A1062.
[5] V. Ramani, R. Kunz, H.J.M. Fenton, J. Power Sources 152 (2005) 182.
[6] E. Yeager, J. Mol. Catal. 38 (1986) 5.
[7] R. Adzic, in: J. Lipkowski, P.N. Ross (Eds.), Electrocatalysis, Wiley-VCH, 1998, p. 197.
[8] W. Liu, D. Zuckerboard, J. Electrochem. Soc. 152 (2005) A1165.
[9] G.G. Scherer, Berichte der Bunsen-Gesellschaft 94 (1990) 1008.
[10] M. Watanabe, H. Uchida, M. Emori, J. Electrochem. Soc. 145 (1998) 1137.
[11] M.R. Tarasevich, A. Sadkowski, E. Yeager, Oxygen Electrochemistry, Plenum Press, New York, 1983.
[12] M. Inaba, H. Yamada, J. Tokunaga, A. Tasaka, Electrochem. Solid-State Lett. 7 (2004) A474.
[13] A.B. Laconti, M. Hamdan, R.C. McDonald, in: W. Vielstich, H.A. Gasteiger, A. Lamn (Eds.), Handbook of Fuel Cells-Fundamentals, Technology and Applications, vol. 3, John Wiley & Sons Ltd., New York, 2003, p. 647.
[14] H. Wang, G.A. Capuano, J. Electrochem. Soc. 145 (1998) 780.
[15] F.N. Buchi, B. Gupta, O. Haas, G.G. Scherer, Electrochim. Acta 40 (1995) 345.
[16] A. Pozio, R.F. Silva, M. De Francesso, L. Giorgi, Electrochim. Acta 48 (2003) 1543.
[17] J. Qiao, M. Saito, K. Hayamizu, T. Okada, J. Electrochem. Soc. 153 (2006) A967.
[18] T. Kinumoto, M. Inaba, Y. Nakayama, K. Ogata, R. Umebayashi, A. Tasaka, Y. Iriyama, T. Abe, Z. Ogumi, J. Power Sources 158 (2006) 1222.
[19] T. Okada, in: W. Vielstich, H.A. Gasteiger, A. Lamn (Eds.), Handbook of Fuel Cells—Fundamentals, Technology and Applications, 3, John Wiley & Sons, New York, 2003, p. 627.
[20] P. Maletzky, R. Bauer, J. Lahnsteiner, B. Pouresmael, Chemosphere 38 (1999) 2315.
[21] E. Niki, Chemistry of Active Oxygen Species, Center of Academic Publications of Japan, Tokyo, 1990.
[22] W.C. Schumb, C.N. Satterfield, R.L. Wentworth, Hydrogen Peroxide, Reinhold Pub. Co., New York, 1955.
[23] D.P. Wilkinson, J. St-Pierre, in: W. Vielstich, H.A. Gasteiger, A. Lamn (Eds.), Handbook of Fuel Cells—Fundamentals, Technology and Applications, vol. 3, John Wiley & Sons, Ltd., New York, 2003, p. 611.
[24] S.D. Knights, K.M. Colbow, J. St-Pierre, D.P. Wilkinson, J. Power Sources 127 (2004) 127.
[25] E. Endoh, S. Terazono, H. Widjaja, Y. Takimoto, Electrochem. Solid-State Lett. 7 (2004) A209.
[26] V.S. Murthi, C.R. Urian, S. Mukerjee, J. Phys. Chem. B 108 (2004) 11011.
[27] R. Liu, E.S. Smotkin, J. Electroanal. Chem. 535 (2002) 49.
[28] R.C. Urian, A.F. Gulla, S. Mukerjee, J. Electroanal. Chem. 554/555 (2003) 307.
[29] R.B. Hodgdon, J.R. Boyack, A.B. LaConti Report TIS 65DE 5, General Electric Company, 1966.
[30] L. Zhang, C. Ma, S. Mukerjee, J. Electroanal. Chem. 568 (2004) 273.
[31] W. Liu, K. Ruth, G. Rusch, J. New. Mater. Electrochem. Syst. 4 (2001) 227.
[32] H.A. Gasteiger, S.S. Kocha, B. Sompalli, F.T. Wagner, Appl. Catal. A 56 (2005) 9.
[33] H.A. Gasteiger, J.E. Panels, S.G. Yan, J. Power Sources 127 (2004) 162.
[34] M.V. Williams, H.R. Kunz, J.M. Fenton, J. Electrochem. Soc. 152 (2005) A635.
[35] Q. Guo, P.N. Pintauro, H. Tang, A. O'Connor, J. Membr. Sci. 154 (1999) 175.
[36] J. Yu, B. Yi, D. Xing, F. Liu, Z. Shao, Y. Fu, H. Zhang, Phys. Chem. Chem. Phys. 3 (2003) 611.
[37] E. Yeager, Electrochim. Acta 29 (1984) 1527.
[38] P. Maletzky, R. Bauer, J. Lahnsteiner, B. Pouresmael, Chemosphere 10 (1999) 2315.
[39] A. Parthasarathy, C.R. Martin, S. Srinivasan, J. Electrochem. Soc. 138 (1991) 916.
[40] K.A. Mauritz, R.B. Moore, Chem. Rev. 104 (2004) 4535.
[41] C. Heitner-Wirguin, J. Membr. Sci. 120 (1996) 1.
[42] H. Gunzler, H.-U. Gremlich, IR Spectroscopy An Introduction, Wiley-VCH, Cambridge, 2002.
[43] C. Ma, L. Zhang, S. Mukerjee, D. Ofer, B. Nair, J. Membr. Sci. 219 (2003) 123.
[44] C. Suryanarayana, M.G. Norton, X-Ray Diffraction A Practical Approach, Plenum Press, New York, 1998.
[45] T.F. Fuller, F.J. Luczak, D.J. Wheeler, J. Electrochem. Soc. 142 (1995) 1752.
[46] S.S. Abd El Rehim, A.A. El Basosi, S.M. El Zein, M.M. Osman, Collect. Czech. Chem. Commun. 59 (1994) 2383.
[47] F.H.B. Lima, M. Janete Giz, E.A. Ticianelli, J. Braz. Chem. Soc. 16 (2005) 328.
[48] S. Mukerjee, S. Srinivasan, J. Electroanal. Chem. 357 (1993) 201.
[49] S. Mukerjee, J. McBreen, S. Srinivasan, Proc-Electrochem. Soc. 95-26 (1996) 38.
[50] J. Roques, A.B. Anderson, V.S. Murthi, S. Mukerjee, J. Electrochem. Soc. 152 (2005) E193.
[51] A.B. Anderson, J. Roques, S. Mukerjee, V.S. Murthi, N.M. Markovic, V. Stamenkovic, J. Phys. Chem. B 109 (2005) 1198.
[52] U.A. Paulus, A. Wokaun, G.G. Scherer, T.J. Schmidt, V. Stamenkovic, V. Radmilovic, N.M. Markovic, P.N. Ross, J. Phys. Chem. B 106 (2002) 4181.
[53] B.N. Grgur, N.M. Markovic, P.N. Ross, Can. J. Chem. 75 (1997) 1465.
[54] U.A. Paulus, T.J. Schmidt, H.A. Gasteiger, R.J. Behm, J. Electroanal. Chem. 495 (2001) 134.
[55] A.J. Bard, L.R. Faulkner, Electrochemical Methods: Fundamentals and Applications, second ed., John Wiley & Sons, Inc., 2001.
[56] K.M. Cable, K.A. Mauritz, R.B. Moore, J. Polym. Sci. B 33 (1995) 1065.

[57] Z. Liang, W. Chen, J. Liu, S. Wang, Z. Zhou, W. Li, G. Sun, Q. Xin, J. Membr. Sci. 233 (2004) 39.
[58] A. Gruger, A. Regis, T. Schmatko, P. Colomban, Vib. Spectrosc. 26 (2001) 215.
[59] C. Heitner-Wirguin, Polymer 20 (1979) 371.
[60] W.Y. Hsu, T.D. Gierke, J. Membr. Sci. 13 (1983) 307.
[61] H.L. Yeager, A. Steck, J. Electrochem. Soc. 128 (1981) 1880.
[62] M. Falk, Can. J. Chem. 58 (1980) 1495.
[63] R.T. Conley, Infrared Spectroscopy, Allyn and Bacon, Inc., Boston, MA, 1972.
[64] A. Eisenberg, H.L. Yeager, Perfluorinated Ionomer Membranes, American Chemical Society, Washington. DC, 1982.
[65] M. Inaba, 14th International Conference on the Properties of Water and Steam in Kyoto, Kyoto, Japan.